

Hydrodynamic Simulations of A Moving Substructure in A Cluster of Galaxies: Cold Fronts and Turbulence Generation

M. Takizawa

Department of Physics, Yamagata University, Yamagata 990-8560, Japan

`takizawa@sci.kj.yamagata-u.ac.jp`

ABSTRACT

We perform three dimensional hydrodynamical simulations of a moving substructure in a cluster of galaxies. We investigate dynamical evolution of the intracluster medium (ICM) in and around the substructure moving radially in the larger cluster's gravitational potential, and its observational consequences. After the substructure passes the larger cluster's center, a bow shock and clear contact discontinuity form in front of it. The contact discontinuity looks like a sharp cold front in the X-ray image synthesized from the simulation results. This agrees with a structure found in 1E 0657-56. The flow structure remains laminar before the first turnaround because the ram-pressure stripping is dominant over the development of Kelvin-Helmholtz instabilities on the boundary between the substructure and the ambient ICM. When a subcluster oscillates radially around the larger cluster's center, both Kelvin-Helmholtz and Rayleigh-Taylor instabilities develop well and the flow structure becomes highly turbulent. Around the turnaround, the subcluster's cold gas is pushed out of its potential well. Therefore, the cold gas component appears to be in front of the subcluster. A relatively blunt cold front appears in the simulated X-ray image because the contact discontinuity is perturbed by Rayleigh-Taylor instabilities. This can explain the ICM structure found in A168.

Subject headings: galaxies: clusters: general — galaxies: clusters: individual (A168, 1E 0657-56) — hydrodynamics — intergalactic medium — X-rays: galaxies: clusters

1. Introduction

Clusters of galaxies are the largest virialized objects in the present universe. In the standard scenario of cosmological structure formation, larger structures form more recently.

Thus, clusters of galaxies are recognized as the virialized objects that form in the most recent epoch, and they are structure formation sites that we can observe in detail at relatively low redshifts. In fact, some clusters are forming now, which is evident from moving substructures found through X-ray observations (e.g., Markevitch et al. 2000, 2002; Vikhlinin et al. 2001b).

Moving substructures cause various characteristic structures in the intracluster medium (ICM). A bow shock and contact discontinuity will form in front of them. The latter most likely corresponds to a “cold front” that is a sharp feature in the X-ray brightness distribution found by *Chandra* in a number of clusters (e.g., Markevitch et al. 2000; Vikhlinin et al. 2001b; Sun et al. 2002; Kempner et al. 2002; Dupke & White 2003). Moving substructures most likely generate turbulence in the ICM through fluid instabilities. Mazzotta et al. (2002) found arc-like filamentary features in the X-ray image of A3667, which are probably produced via hydrodynamic instability. Turbulence plays crucial roles in cluster evolution. It may have a significant impact on the transport and mixture of the heavy elements and thermal energy. Fluid turbulence generates magnetic turbulence, which accelerates non-thermal particles and causes various high energy phenomena in the intracluster space (e.g., Ohno et al. 2002; Fujita et al. 2003; Brunetti et al. 2004). *Astro-E2* satellite, which is planned to be launched in 2005, will detect broadened lines due to the turbulent motion (Sunyaev et al. 2003; Fujita et al. 2005; Pawl et al. 2005). In order to study above-mentioned issues, it is crucial to clarify the generation processes and structure of the ICM turbulence.

Numerical simulations are necessary to investigate the ICM structure and evolution in detail. In fact, highly turbulent ICM and structures similar to cold fronts have been found in N-body + hydrodynamical simulations with cosmological initial conditions (e.g., Bialek et al. 2002; Nagai & Kravtsov 2003; Sunyaev et al. 2003; Mathis et al. 2005; Tittley & Henriksen 2005). It is true that such simulations are useful in order to investigate ICM evolution as a whole in realistic situations. In such simulations, however, it is often difficult to derive clear physical interpretations, to control initial conditions for some purposes, and to achieve very high resolution in particular interesting regions efficiently. Therefore, simulations with a little bit less realistic but idealized and well-controlled conditions are complementary and useful. For example, some study cluster mergers (Roettiger et al. 1996; Takizawa 1999, 2000; Ricker & Sarazin 2001; Ritchie & Thomas 2002), and others deal with ICM dynamics near moving substructures (Heinz et al. 2003; Asai et al. 2004). Such simulations are suitable in order to clarify physical processes concerned, compare simulation results with specific observations, achieve very high resolution efficiently in the region concerned, and so on.

In this paper, we adopt the latter approach in order to follow flow evolution in and around a moving substructure with high spatial resolution. This is necessary especially to investigate the structure and generation processes of the turbulence. Because the field of

view of *Astro-E2* XRS is not so large, detailed flow velocity structure information obtained from numerical simulations is very important to predict (and/or interpret) *Astro-E2* XRS observations and study ICM dynamics. In particular, information about when and where turbulence occurs is useful. We perform three dimensional hydrodynamical simulations of a moving substructure in a cluster of galaxies. To emulate the time-dependent environment near the moving subcluster in the larger cluster, we take account of the time evolution of the boundary conditions in front of the subcluster. We calculate the subcluster’s position and velocity relative to the larger cluster with an approximation that the subcluster is a test particle in the larger cluster’s gravitational potential. We take this information into account calculating the boundary conditions in front of the subcluster in our hydrodynamical simulations.

The rest of this paper is organized as follows. In §2 we describe the adopted numerical methods and initial conditions for our simulations. In §3 we present the results. In §4 we discuss a turbulence generation scenario by substructure motion based on our simulation results. In §5 we compare our results with X-ray observations of 1E 0657-56 and A168. In §6 we summarize the results and discuss their implications.

2. The Simulations

2.1. Numerical Methods

In the present study, we use the Roe TVD scheme to follow the dynamical evolution of the ICM (see Hirsch 1990). The Roe scheme is a Godunov-type method with a linearized Riemann solver (Roe 1981). It is relatively simple and good at capturing shocks without any artificial viscosity. Using the MUSCLE approach and a minmod TVD limiter, we obtain second-order accuracy without any numerical oscillations around discontinuities. To avoid negative pressure, we solve the equations for the total energy and entropy conservation simultaneously. This method is often used in astrophysical hydrodynamical simulations where high Mach number flow can occur (Ryu et al. 1993; Wada & Norman 2001).

We focus on the flow evolution in the region near the subcluster moving in the larger cluster. We calculate the evolution of the subcluster’s position and velocity relative to the larger cluster with an approximation that subcluster is a test particle in the larger cluster’s gravitational potential. Only gravitational interaction is considered between them. The larger cluster’s potential is fixed in space. The subcluster’s potential is fixed in shape, with the center of the subcluster’s potential moving in the potential of the larger cluster as a test particle would. The gas is not self-gravitating so simply responds to the sum of the

larger cluster and subcluster potentials. We set a simulation box in a frame comoving with the subcluster. The coordinate system is set so that the subcluster’s center is always at the origin and the larger cluster’s ICM approaches the subcluster from the $+x$ side initially. Hydrodynamic calculations are performed only inside this box. Taking account of the position and velocity relative to the larger cluster, we make the boundary conditions in front of the subcluster change with time. Free boundary conditions are adopted for the other boundaries. We assume that the presence of the subcluster does not affect the properties of the larger cluster outside the simulation box such as its gravitational potential shape, ICM density structure, and ICM temperature structure. Gradients of the larger cluster’s physical quantities in the direction perpendicular to the subcluster’s motion are neglected inside the simulation box.

2.2. Models and Initial Conditions

We assume that both the subcluster and larger cluster are represented by a conventional isothermal beta-model in the initial state. The gravitational potential distribution is that of a King model for each cluster. The density distribution and mass inside the radius r of a King model are

$$\rho(r) = \rho_0(1 + x^2)^{-3/2}, \quad (1)$$

$$M(r) = 4\pi\rho_0r_c^3[\ln\{x + (1 + x^2)^{1/2}\} - x(1 + x^2)^{-1/2}], \quad (2)$$

where $x = r/r_c$. Here, ρ_0 and r_c are the central density and core radius, respectively. The gravitational mass distribution is assumed to be dominated by the dark matter (DM) component. We set the outer boundary of the DM distribution to $5r_c$. Thus, the total mass M can be used as a model parameter, instead of the central density ρ_0 . We set $r_c = 200$ kpc and $M = 8.57 \times 10^{14} M_\odot$ for the larger cluster, and $r_c = 40$ kpc and $M = 1.43 \times 10^{14} M_\odot$ for the subcluster. The ICM is assumed to be in hydrostatic equilibrium with isothermal temperature distribution within the DM potential. In the isothermal beta-model, the gas density distribution is

$$\rho_g(r) = \rho_{g,0}(1 + x^2)^{-3\beta/2}, \quad (3)$$

where $\rho_{g,0}$ and β are the central gas density and the specific energy ratio of the dark matter to the gas, respectively. We set the initial temperature so that $\beta = 0.8$ for each cluster. The mass density of the gas is assumed to be a tenth of that of the DM in the center. The size of the simulation box and the number of the grid points are $(800 \text{ kpc})^3$ and 400^3 , respectively.

We show the results for two representative cases. In one case, the subcluster falls radially into the larger cluster from the outskirts, crosses the center, and reaches the opposite side

of the larger cluster. We call this “the radial infall model”. In the other case, the subcluster is oscillating near the bottom of the larger cluster’s gravitational potential well. We call this “the sloshing model”. Figure 1 shows the time evolution of the subcluster’s position, velocity, and Mach number relative to the larger cluster for the radial infall model. In this model, the subcluster is at rest 1 Mpc away from the larger cluster’s center in the initial state. We follow the subcluster’s motion for 1 Gyr until it reaches about 0.8 Mpc away from the center on the opposite side of the initial position. Figure 2 shows the same as figure 1, but for the sloshing model. In this model, the subcluster is at rest 0.5 Mpc away from the center initially. We follow its motion for 1.8 Gyr. The subcluster crosses the larger cluster’s center three times.

3. Results

Figure 3 shows snapshots of the density and temperature distribution on the $z = 0$ surface at $t = 0.56, 0.67, 0.78, 0.89$, and 1.0 Gyr of the radial infall model. The upper and lower panels show the density and temperature distribution, respectively. The subcluster starts to fall at $t = 0$, and is accelerated towards the larger cluster center. Both the relative velocity and the density in front of the subcluster are increasing. Therefore, the subcluster suffers increasing ram pressure, which is the product of the density and the square of the relative velocity. As a result, the subcluster’s ICM is gradually stripped off in the outer region. The forward and reverse shocks are seen in the density and temperature distribution at $t = 0.58$ and 0.67 Gyr. The reverse shock cannot penetrate into the substructure’s core. Thus, a cold remnant survives. The temperature becomes higher between the two shocks, especially just behind the reverse shock. The subcluster reaches the larger cluster’s center at $t \sim 0.64$ Gyr. Small eddy-like structures develop on the boundary between the substructure and the surrounding gas through Kelvin-Helmholtz instabilities. After the substructure passes the larger cluster’s center, the cold remnant of the substructure is decelerating and enters the lower density region. Therefore, it suffers the decreasing ram pressure and no more gas is stripped off. A bow shock and contact discontinuity are clearly seen in front of the remnant. Although the small eddies are generated through Kelvin-Helmholtz instabilities, the flow structure is basically laminar in the radial infall model.

Figure 4 shows the same as figure 3, but for the sloshing model. The snapshots at $t = 0.8, 1.0, 1.2, 1.4$, and 1.6 Gyr are presented. In this model, the subcluster is at rest 0.5 Mpc away from the larger cluster’s center in the initial state. It first passes the center at $t \sim 0.33$ Gyr, reaches 0.5 Mpc away from the center on the opposite side, and turns around at $t \sim 0.65$ Gyr. Then it falls back again, crosses the center at $t \sim 0.98$ Gyr, reaches the initial

position at $t \sim 1.3$ Gyr, and turns around again. Figure 4 shows the evolution from the first turnaround to the second one. At $t = 0.8$ Gyr the subcluster has already passed the larger cluster’s center and turned around. A mushroom-like structure forms because of the ram pressure and Kelvin-Helmholtz instabilities. Furthermore, another mushroom-like structure forms inside the first one after the turn around. After the second passage of the main cluster’s center, a bow shock forms again in front of the substructure ($t = 1.2$ Gyr). Acceleration toward the the larger cluster center acts on the substructure in the larger cluster’s potential. This means that the inertial force in the $+x$ direction as well as the gravitational force of the subcluster act on the gas inside the subcluster in the frame comoving with the subcluster. If the former is stronger than the latter, the effective gravity is in the $+x$ direction. Therefore, the gas in the region of $x > 0$ is accelerated towards the outside of the subcluster potential, rather than its center. Because the denser gas is located nearer the center, Rayleigh-Taylor instabilities develop at the bow shock and contact discontinuity. As a result, cold gas seems to be in front of the subcluster’s center ($t = 1.4$ Gyr). Finally, the cold cloud breaks into small pieces and the flow becomes highly turbulent ($t = 1.6$ Gyr).

4. A Turbulence Generation Scenario

Let us discuss a turbulence generation scenario by moving substructures in clusters of galaxies based on the results mentioned above. When a subcluster falls into a larger cluster almost radially, a situation similar to the radial infall model is realized before the first turnaround. The gas in the outer region is stripped off because of the ram pressure, but Kelvin-Helmholtz instabilities hardly develop on the boundary. Therefore, the flow structure remains laminar in this stage.

Then, the substructure experiences the first turnaround and falls back again. If the gravitational reaction of the substructure to the larger cluster is negligible (or, if the test particle assumption is very good), the substructure keeps oscillating with a constant amplitude in the larger cluster’s potential. However, the test particle assumption is not good for a longer timescale. Because of dynamical friction, the oscillation amplitude decreases and the substructure gradually sinks into the larger cluster’s center. Therefore, the situation like the sloshing model occurs. As we showed in §3, both Kelvin-Helmholtz and Rayleigh-Taylor instabilities grow well, and the substructure is destroyed and mixed into the ambient gas. In this stage, the flow structure becomes highly turbulent.

5. Comparison with 1E 0657-56 and A168

5.1. 1E 0657-56

1E0657-56 is one of the most well-known examples of a merging cluster. It is the hottest known cluster and has a very powerful radio halo (Liang et al. 2000). There are two peaks in both the X-ray surface brightness distribution (Tucker et al. 1998; Markevitch et al. 2002) and galaxy distribution (Barrena et al. 2002), but their positions do not agree with each other. Observations of the line-of-sight velocities of the member galaxies suggest that its collision axis is almost perpendicular to the line-of-sight (Barrena et al. 2002). Markevitch et al. (2002) shows the detailed analysis of the *Chandra* observations. A clear cold front and possible bow shock are found in the west of the western smaller X-ray peak. Temperature is higher between the cold front and possible bow shock.

Figure 5 shows the X-ray surface brightness distribution (contours) and emissivity-weighted temperature map (colors) of the radial infall model at $t = 0.89$ Gyr. The surface brightness contours are spaced by a factor of 2.2. We assume that the volume emissivity is proportional to the $\rho_g^2 T_g^{1/2}$, where ρ_g and T_g are the gas density and temperature, respectively. The line of sight is perpendicular to the substructure motion, and the integrations are carried out within the simulation box. In this simulated X-ray image, we can see two discontinuities in front of the X-ray peak. The emissivity-weighted temperature is higher between those discontinuities, and is the lowest at the X-ray peak itself. At the discontinuity nearer to the peak, the emissivity-weighted temperature is lower in the brighter side, and vice versa. This means that the contact discontinuity in front of the substructure will be recognized as a cold front in the X-ray observations. As for the overall ICM structures of 1E0657-56 around the west X-ray peak, our results nicely agree with the X-ray observations.

Clowe et al. (2004) investigated the mass distribution of 1E0657-56 by weak gravitational lensing. They show clear offsets of the mass density peaks from the X-ray ones, and that the mass distribution is well similar to the galaxy one. The smaller substructure in mass is ahead of the X-ray one. They argue that this structure occurs because ICM experiences ram pressure but DM and galaxies do not during cluster mergers. In contrast with this, our results hardly show such an offset of the X-ray peak from the potential center that is always at the center of the simulation box. Evidently, it is necessary to search wider parameter space in order to clarify if their interpretation is valid. There might be a feasible parameter set to realize such a situation. However, this is not within a scope of this paper. We should note that the dynamical evolution of the dark matter component is not fully calculated self-consistently in our simulations. As a result, the gravitational potential of the substructure is not modified at all. Obviously, this is not true in actual clusters. This likely affects the

condition of ram pressure stripping. It will be useful to search wider parameter space with high resolution N-body + hydrodynamical simulations.

5.2. A168

A168 is a cool irregular cluster. Its X-ray structure is highly elongated (Ulmer et al. 1992; Jones & Forman 1999), and two galaxy subclusters are located in its ends. Recently, Hallman & Markevitch (2004) revealed the detailed ICM density and temperature structures around the northern subcluster. They found the coolest ICM component in the north of the northern subcluster. This structure is qualitatively different than what is found in 1E0657-56. They also show that the tip of the coolest component consists of a cold front and that its edge is not so sharp as other examples (e.g., Markevitch et al. 2000; Vikhlinin et al. 2001b).

Figure 6 shows the same as in figure 5, but for the sloshing model at $t = 1.4$ Gyr. The surface brightness contours are spaced by a factor of 1.6. The coldest component of the ICM appears to be located in front of the X-ray peak. This configuration is qualitatively the same as what is found around the northern subcluster of A168. At the front edge of the cold component, the denser side is colder, and vice versa. Thus, this will be recognized as a cold front in actual X-ray observations. In addition, this edge is not so sharp as that in figure 5, which is consistent with the *Chandra* results of A168 (Hallman & Markevitch 2004). This is because the contact discontinuity itself is being perturbed through Rayleigh-Taylor instabilities. As figure 4 shows, the cold component in A168 would be break into pieces and mixed into the ambient ICM in the future.

6. Summary and Discussion

We investigate the gas motion in and around a moving substructure in a cluster of galaxies using the three dimensional Roe-TVD hydrodynamic code. The subcluster’s relative motion in the larger cluster is calculated assuming that the subcluster is a test particle in the larger cluster’s gravitational potential. We take account of the time variation of the ICM density and pressure in front of the subcluster, and the velocity relative to the larger cluster. Two representative cases are calculated. One is a simple radial infall of the subcluster (the radial infall model). The other is a radial oscillation around the larger cluster’s center (the sloshing model).

In the radial infall model, a clear bow shock and contact discontinuity form in front of the subcluster. Kelvin-Helmholtz instabilities hardly develop because the boundary between the

substructure and the surrounding ICM is not stable because of the ram pressure stripping. As a result, the flow structure remains laminar before the first turnaround. In the sloshing model, on the other hand, the flow structure becomes highly turbulent. In addition to Kelvin-Helmholtz instabilities, Rayleigh-Taylor instabilities develop well around the turnaround.

We compare our results with *Chandra* observations of 1E0657-56 and A168. The X-ray surface brightness distribution and emissivity-weighted temperature map synthesized from the simulation data of the radial infall model are in quite good agreement with the X-ray data of 1E0657-56. In contrast to the weak lensing analysis, however, the offset of the X-ray peak from the DM potential well is not seen in our results. As for A168, the X-ray data synthesized from the radial infall model qualitatively agree with the *Chandra* results. The relatively blunt cold front in A168 is probably because of a contact discontinuity perturbed by Rayleigh-Taylor instabilities.

In this work, we neglected the magnetic field in the ICM. However, it is possible that the magnetic field plays a crucial role to suppress the development of Kelvin-Helmholtz instabilities (Asai et al. 2004). The magnetic field along the boundary layer probably works to maintain the smaller subcluster’s gas to be a distinct structure after it is stripped off the DM potential. Dynamical motion of the substructure itself possibly produces such kind of magnetic field configurations (Vikhlinin et al. 2001a; Asai et al. 2004). It will be useful to perform three dimensional high resolution magnetohydrodynamical simulations in order to investigate detailed evolution. In addition, temperature gradients in the boundary layer possibly produce the magnetic field structure through plasma instabilities (Okabe & Hattori 2003).

Numerical computations were carried out on VPP5000 at the Astronomical Data Analysis Center, ADAC, of the National Astronomical Observatory of Japan. M. T. was supported in part by a Grant-in-Aid from the Ministry of Education, Science, Sports, and Culture of Japan (16740105)

REFERENCES

- Asai, N., Fukuda, N., & Matsumoto, R. 2004, *ApJ*, 606, L105
- Barrena, R., Biviano, A., Ramella, M., Falco, E. E., & Seitz, S. 2002, *A&A*, 386, 816
- Bialek, J. J., Evrard, A. E., & Mohr, J. J. 2002, *ApJ*, 578, L9
- Brunetti, G., Blasi, P., Cassano, R., & Gabici, S. 2004, *MNRAS*, 350, 1174

- Clowe, D., Gonzalez, A., & Markevitch, M. 2004, *ApJ*, 604, 596
- Dupke, R., & White, R. E. 2003, *ApJ*, 583, L13
- Fujita, Y., Takizawa, M., & Sarazin, C., L. 2003, *ApJ*, 584, 190
- Fujita, Y., Matsumoto, T., Wada, K., & Furusho, T. 2005, *ApJ*, 619, L139
- Hallman, E., J., & Markevitch, M. 2004, *ApJ*, 610, L81
- Heinz, S., Churazov, E., Forman, W., Jones, C., & Briel, U. G. 2003, *MNRAS*, 346, 13
- Hirsch, C. 1990, *Numerical Computation of Internal and External Flows* (New York: John Wiley & Sons)
- Jones, C., & Forman, W. 1999, *ApJ*, 511, 65
- Kempner, J. C., Sarazin, C. L., & Ricker, P. M. 2002, *ApJ*, 579, 236
- Liang, H., Hunstead, R. W., Birkinshaw, M., & Andreani, P. 2000, *ApJ*, 544, 686
- Markevitch, M., et al. 2000, *ApJ*, 541, 542
- Markevitch, M., et al. 2002, *ApJ*, 567, L27
- Mathis, H., Lavaux, G., Diego, J. M., & Silk, J. 2005, *MNRAS*, 357, 801
- Mazzotta, P., Fusco-Femiano, R., & Vikhlinin, A. 2002 *ApJ*, 569, L31
- Nagai, D., & Kravtsov, A. V. 2003, *ApJ*, 587, 514
- Ohno, H., Takizawa, M., & Shibata, S. 2002 *ApJ*, 577, 658
- Okabe, N., & Hattori, M. 2003, *ApJ*, 599, 964
- Pawl, A., Evrard, A. E., & Dupke, R. A. 2005, *ApJ*, submitted (astro-ph/0503281)
- Ricker, P. M., & Sarazin, C. L. 2001, *ApJ*, 561, 624
- Ritchie, B. W., & Thomas, P. A. 2002, *MNRAS*, 329, 675
- Roe, P. L. 1981, *J. Comput. Phys.*, 43, 357
- Roettiger, K., Burns, J. O., & Loken, C. 1996, *ApJ*, 473, 651
- Ryu, D., Ostriker, J. P., Kang, H., & Cen, R. 1993, *ApJ*, 414, 1

- Sun, M., Murray, S. S., Markevitch, M., & Vikhlinin, A. 2002, *ApJ*, 565, 867
- Sunyaev, R. A., Norman, M. L., & Bryan, G. L. 2003, *Astronomy Letters*, 29, 783
- Takizawa, M. 1999, *ApJ*, 520, 514
- Takizawa, M. 2000, *ApJ*, 532, 183
- Tittley, E. R., & Henriksen, M. 2005, *ApJ*, 618, 227
- Tucker, W., et al. 1998, *ApJ*, 496,
- Ulmer, M. P., Wirth, G. D., & Kowalski, M. P. 1992, *ApJ*, 397, 430
- Vikhlinin, A., Markevitch, M., & Murray, S. S. 2001a, *ApJ*, 549, L47
- Vikhlinin, A., Markevitch, M., & Murray, S. S. 2001b, *ApJ*, 551, 160
- Wada, K., & Norman, C., A. 2001, *ApJ*, 547, 172

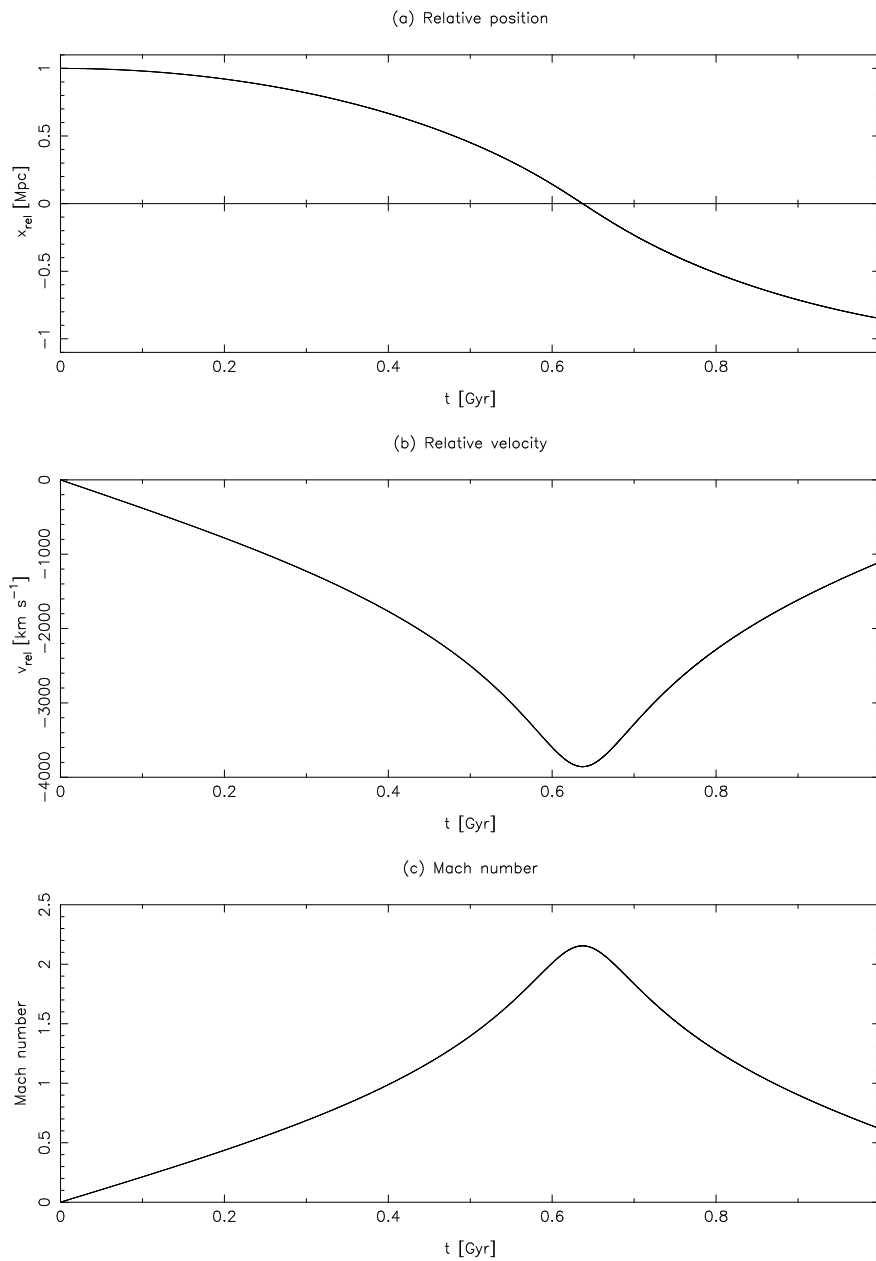


Fig. 1.— Time evolution of the subcluster’s (a) position, (b) velocity, and (c) Mach number relative to the larger cluster’s center for the radial infall model.

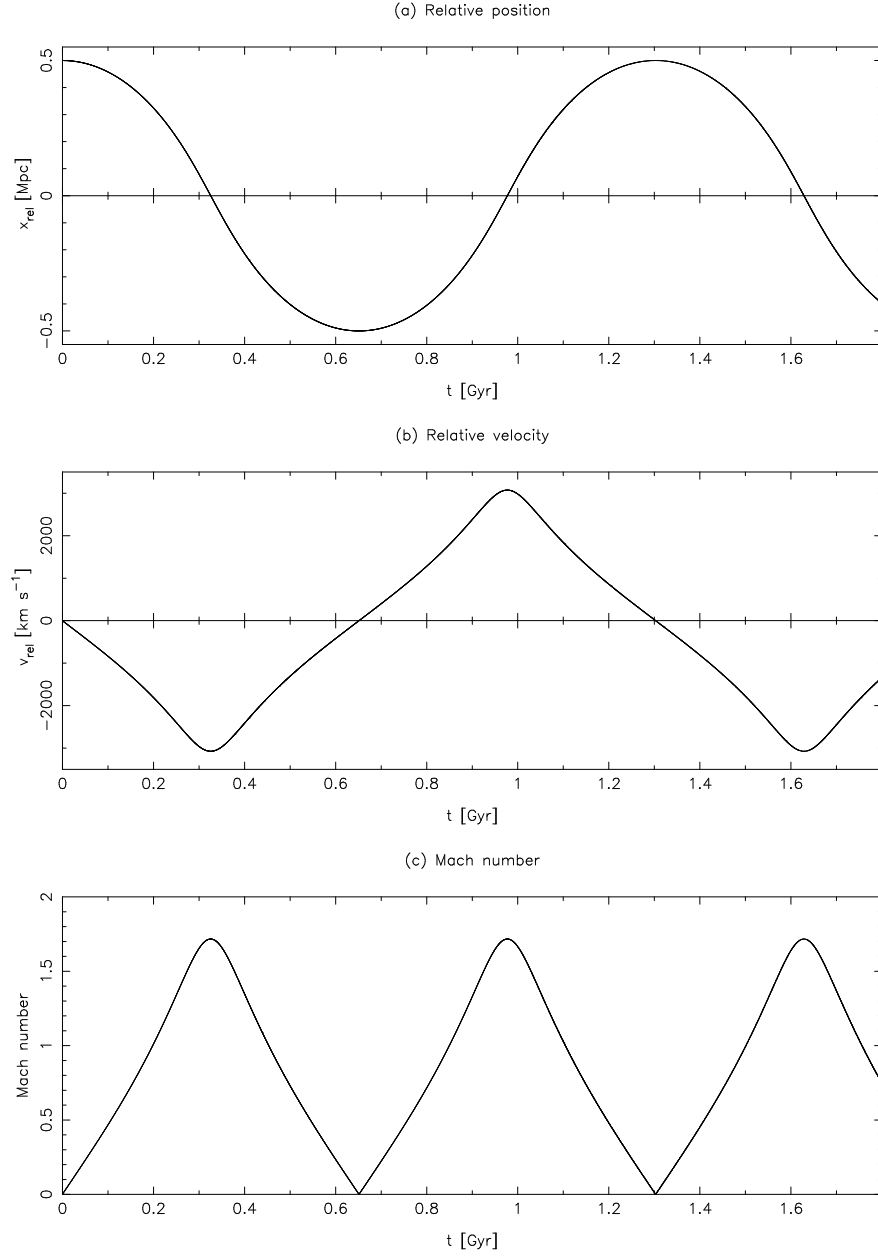


Fig. 2.— The same as figure 1, but for the sloshing model.

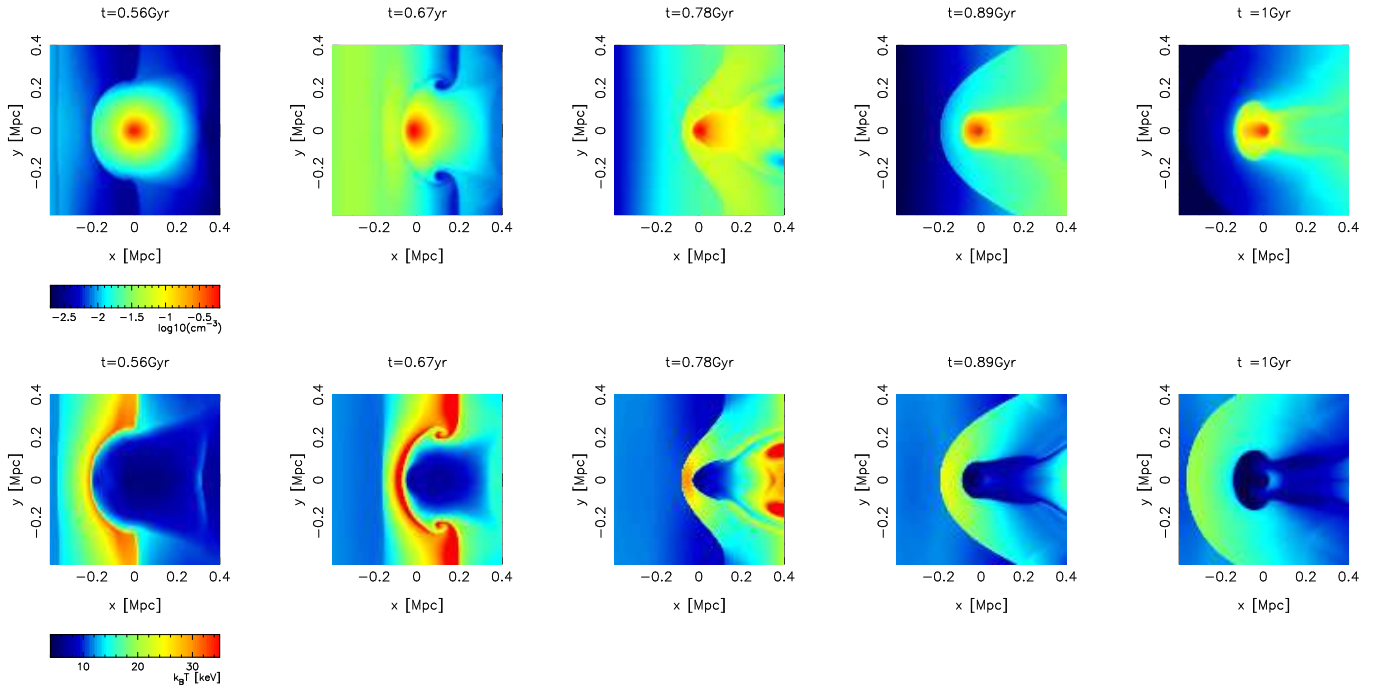


Fig. 3.— Upper panels show snapshots of the density distribution on the $z = 0$ surface at $t = 0.56, 0.67, 0.78, 0.89$, and 1.0 Gyr of the radial infall model. Lower panels show the same ones but for the temperature distribution.

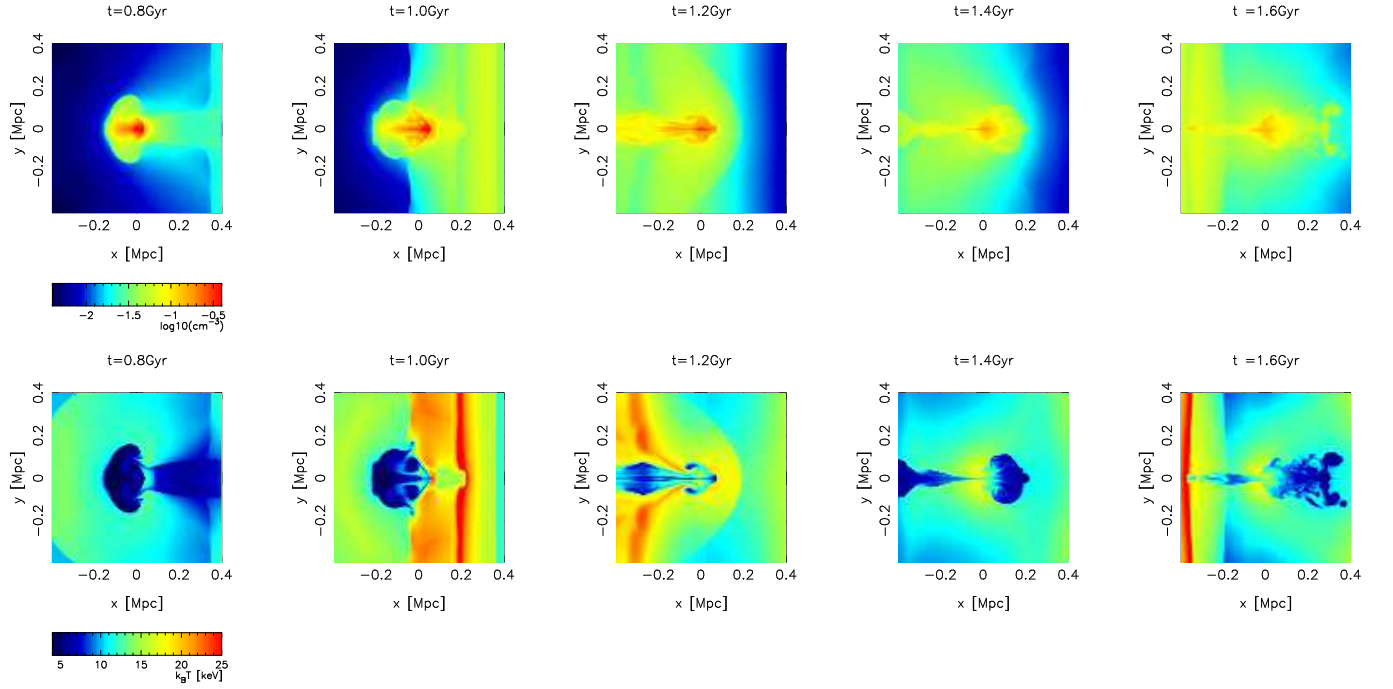


Fig. 4.— The same as figure 3, but for the sloshing model. The snapshots at $t = 0.8, 1.0, 1.2, 1.4,$ and 1.6 Gyr are presented.

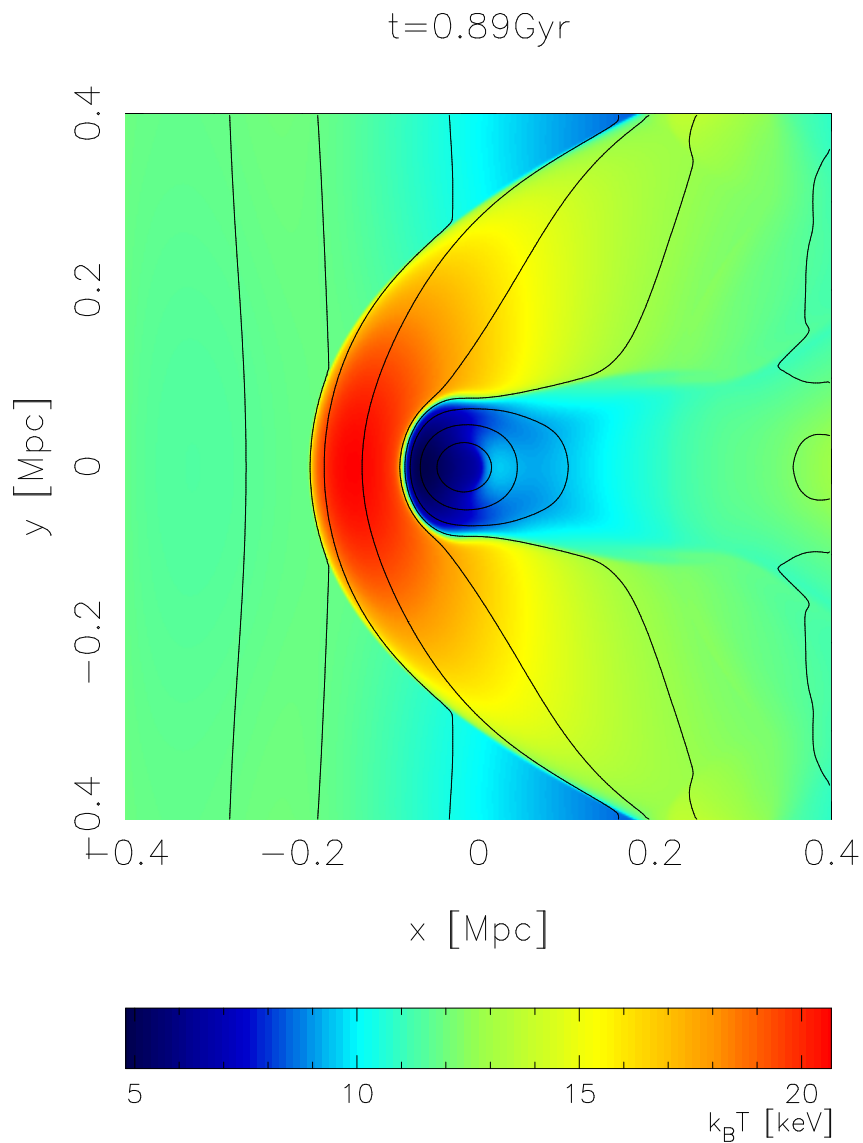


Fig. 5.— The X-ray surface brightness distribution (contours) and emissivity-weighted temperature map (colors) for the radial infall model at $t = 0.89\text{ Gyr}$. The surface brightness contours are spaced by a factor of 2.2. The line-of-sight is assumed to be perpendicular to the substructure motion.

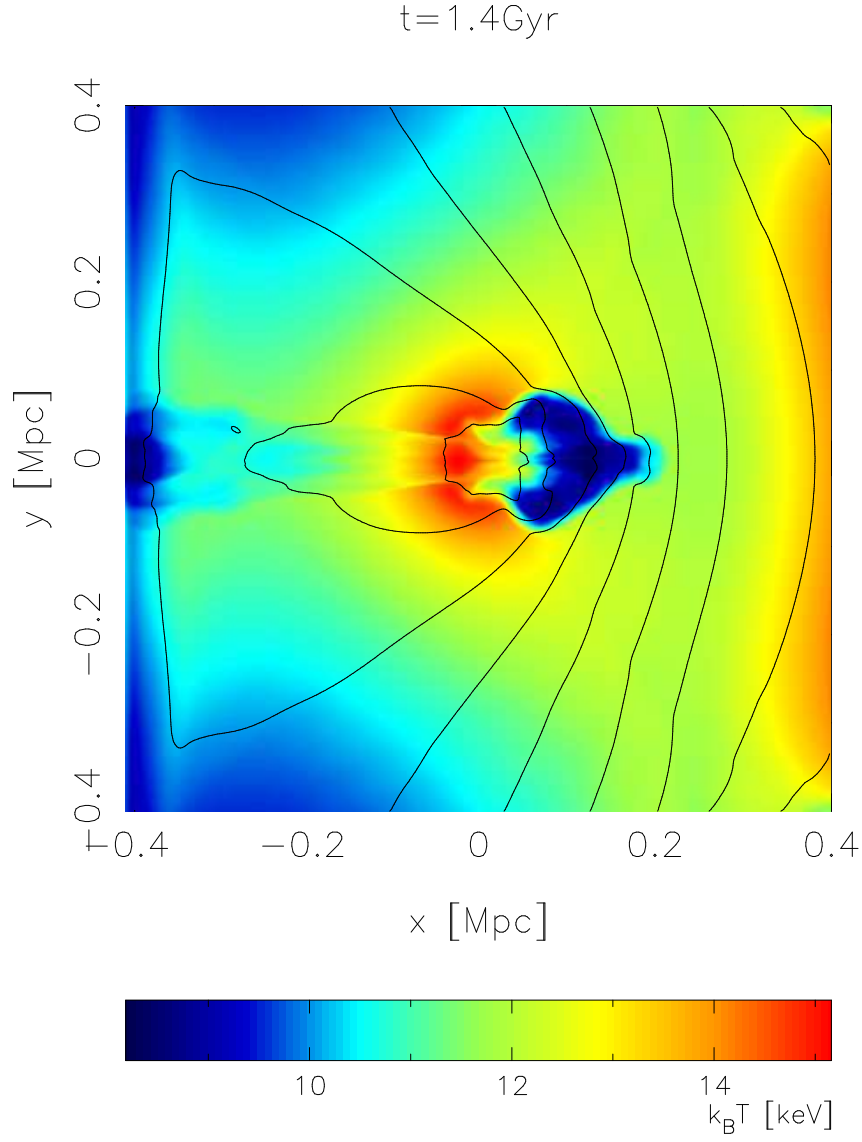


Fig. 6.— The same as in figure 5, but for the sloshing model at $t = 1.4 \text{ Gyr}$. The surface brightness contours are spaced by a factor of 1.6.